

pubs.acs.org/NanoLett Letter

# Dynamics of the Chemically Driven Densification of Barium Titanate Using Molten Hydroxides

Arnaud Ndayishimiye,\*<sup>,†</sup> Mert Y. Sengul,<sup>†</sup> Dooman Akbarian, Zhongming Fan, Kosuke Tsuji, Sun Hwi Bang, Adri C. T. van Duin, and Clive A. Randall



Cite This: Nano Lett. 2021, 21, 3451-3457



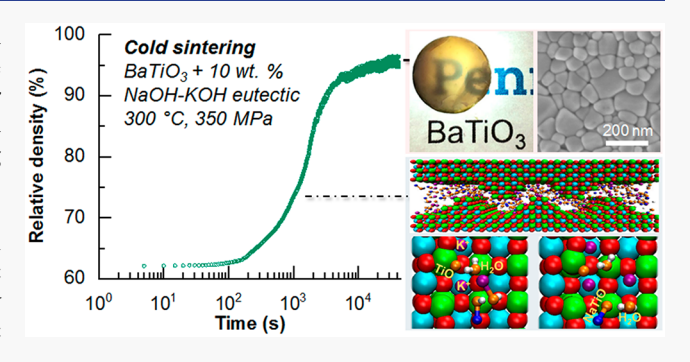
**ACCESS** I

III Metrics & More

Article Recommendations

Supporting Information

ABSTRACT: Molten hydroxides, often used for crystal growth and nanoparticle synthesis, have recently been applied for the single step densification of several inorganic materials under moderate uniaxial pressures and 1000 °C below their usual sintering temperatures. The latter approach, termed cold sintering process (CSP), is a mechanochemically driven process that enables the densification of inorganic materials through a dissolution–precipitation creep mechanism. In this study, we report the main densification mechanisms of BaTiO<sub>3</sub> in a NaOH-KOH eutectic mixture. A chemical insight at the atomistic level, investigated by ReaxFF molecular dynamics simulations, offers plausible ionic complex formation scenarios and reactions at the BaTiO<sub>3</sub>/molten



hydroxide interface, enabling the dissolution-precipitation reactions and the subsequent cold sintering of BaTiO<sub>3</sub>.

KEYWORDS: cold sintering, molten salts, inorganic materials, ReaxFF, molecular dynamics

## **■ INTRODUCTION**

Sintering is generally referred to as a thermally driven process occurring at a temperature  $T > 0.5T_{\rm m}$  (where  $T_{\rm m}$  is melting temperature) to allow the densification of a powder compact through surface or volume atomic diffusion mechanisms.<sup>1,2</sup> This consideration is true, except for the cold sintering process (CSP), a chemically driven sintering process that can occur at  $T < 0.2T_{\rm m}$  through the pressure solution creep mechanism. Pressure solution, often encountered in structural geology, is fluid-assisted stress-driven mass transport<sup>3-5</sup> enabled by chemical potential gradients between highly stressed solidsolid contacts and little stressed pore surfaces (Figure S1). The CSP recently drew a lot of attention, as it is an energy- and cost-efficient technique that enabled the low-temperature densification of ceramics and several ceramic-based composites at temperatures lower than 400 °C.6-10 Like CSP, other processes such as cool SPS (spark plasma sintering), 11-13 hydrothermal sintering, 14-17 and RTS (room-temperature sintering)<sup>18,19</sup> are based on the use of moderate heat, uniaxial pressure, and an enabling transient chemistry to promote pressure solution mechanisms.

Although aqueous solvents, organic acids and polar solvents, chelating agents, and hydrated organics are mainly used in this process, occasionally metastable grain boundaries result and require a secondary heat treatment to achieve highly functional properties. Molten hydroxides, which are generally used for crystal growth and nanoparticle synthesis, of several used recently for the single-step densification of several

inorganic materials such as BaTiO3, SrTiO3, CeO2, ZnO, Bi<sub>2</sub>O<sub>3</sub>, WO<sub>3</sub>, CuO, MnO, (K<sub>x</sub>Na<sub>1-x</sub>)NbO<sub>3</sub> (KNN), and NASICON-type structures. Relative densities above 90–95% and functional properties within similar performances to those observed with materials processed with other sintering techniques, but at temperatures up to 1000 °C lower. This approach represents a major breakthrough in sintering science and can be extended to several other inorganic materials as a cost- and energy-efficient process. 9,27,28 which also enables the fabrication of high-performance functional devices at record low temperatures.<sup>29-31</sup> In spite of widespread use of molten salts for synthesis and crystal growth in both open or closed systems (as hydrothermal molten salt (HyMoS)<sup>32</sup> or hydroflux<sup>33</sup> when mixed with approximately 30-40 wt % water), fundamental knowledge of chemical mechanisms is still limited as the use of in situ structural characterization techniques in this environment is still a challenge.<sup>21</sup>

This study aims to improve the fundamental knowledge of densification mechanisms with a chemical perspective in cold sintering using molten salts, and the investigated material system is barium titanate, BaTiO<sub>3</sub> (BTO). BTO is a very

Received: January 6, 2021 Revised: April 9, 2021 Published: April 14, 2021





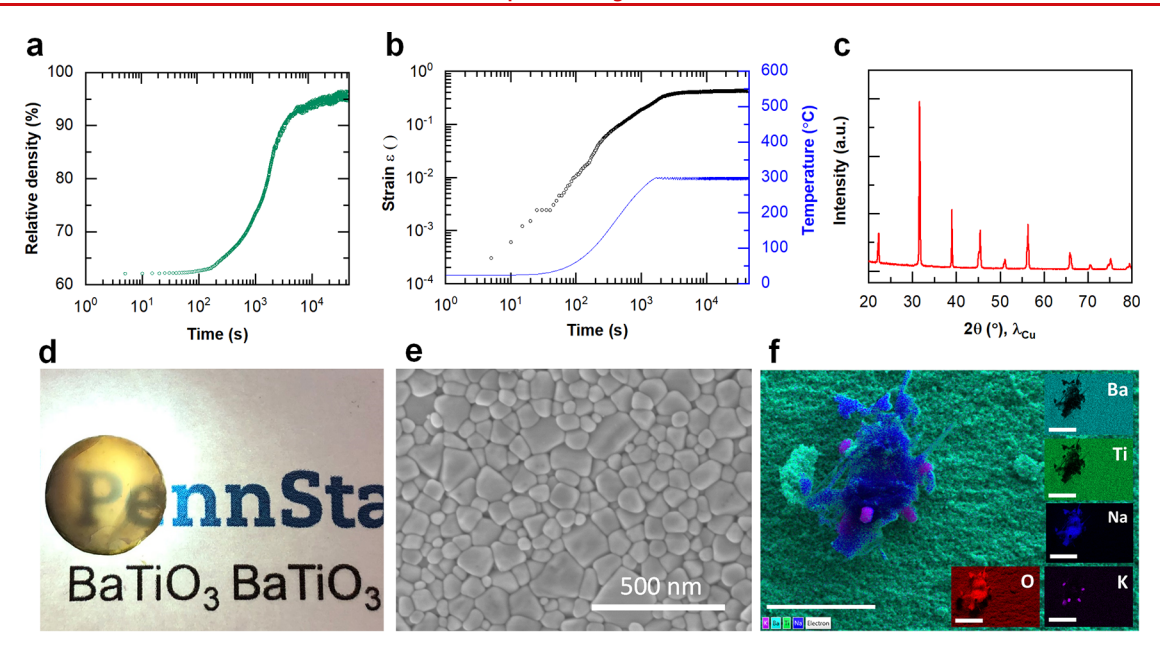


Figure 1. BTO's time-dependent evolution of the (a) relative density (semilog plot) and (b) strain  $\varepsilon$  (log–log plot) during CSP at 300 °C and 350 MPa. (c) X-ray diffraction, (d) photograph highlighting translucency. Credit: The Pennsylvania State University/Dr. Kosuke Tsuji. (e) High-resolution scanning electron microscopy (HR-SEM) and (f) scanning electron microscopy (SEM)—energy-dispersive spectroscopy (EDS) analysis of the as-cold sintered BTO ceramic. The SEM-EDS image in f was obtained with simultaneous acquisition of secondary electron image and elemental maps of barium (Ba), titanium (Ti), sodium (Na), potassium (K), and oxygen (O). Scale bar: 10  $\mu$ m.

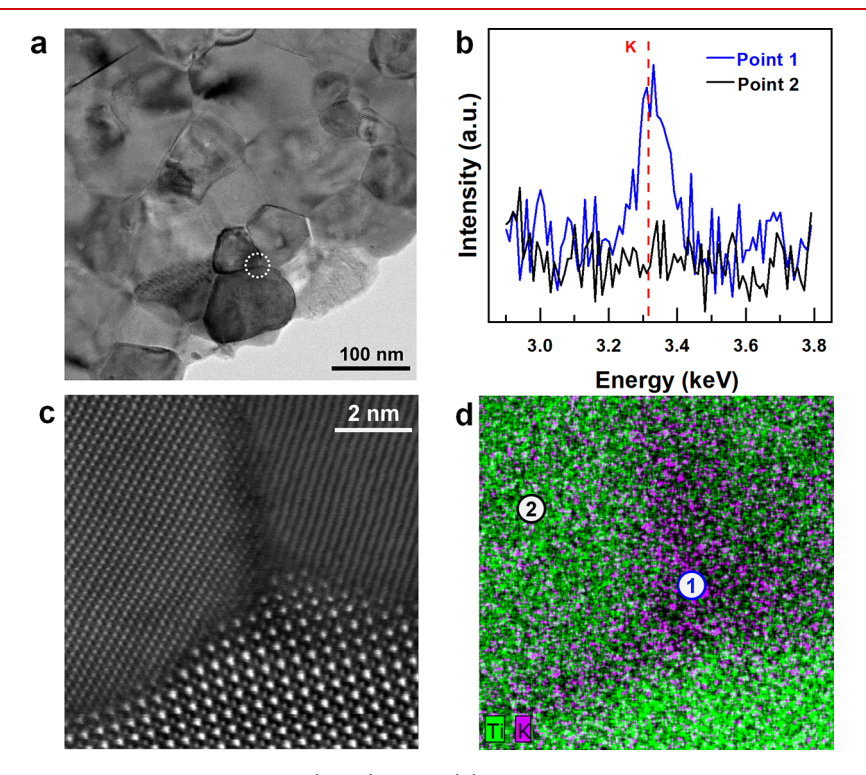


Figure 2. (a) Bright-field transmission electron microscopy (TEM) image, (b) EDS spectra highlighting the presence of potassium (K) element in point 1 and point 2 shown in figure d, (c) high-angle annular-dark-field scanning transmission electron microscopy (HAADF-STEM), and the corresponding (d) scanning transmission electron microscopy—energy-dispersive spectroscopy (STEM-EDS) mapping of a triple junction in BTO.

important dielectric material with high permittivity,  $^{34}$  used to fabricate 4 trillion multilayer ceramic capacitors (MLCC) every year and with 8% annual growth. The sintering process is typically conducted to enable the cofiring with Ni inner electrodes, and therefore in a partially reducing atmosphere at 1200 °C or higher. There is a need to continue to improve the reliability of BaTiO<sub>3</sub>-based dielectrics that is limited by the

electromigration of oxygen vacancies. With a new process such as cold sintering, there are new opportunities to improve the performance of high permittivity dielectrics. We recently established a low-temperature densification of  $\rm BaTiO_3$  (BTO), using a molten NaOH/KOH eutectic (51/49 mol %) hydroxide system at 300 °C and under a uniaxial pressure of 350 MPa.

Given the success of our recent establishment, we report here the main densification mechanisms of BaTiO<sub>3</sub> in a NaOH-KOH eutectic mixture. A chemical insight at the atomistic level, investigated by ReaxFF molecular dynamics, demonstrates a plausible scenario of the BaTiO<sub>3</sub>/molten hydroxide interface-coupled dissolution—precipitation reactions and the subsequent dissociation of the hydroxide mixture.

#### ■ RESULTS AND DISCUSSION

Densification of BaTiO<sub>3</sub> with a NaOH-KOH Eutectic Flux. The densification behavior of BTO in molten hydroxides was first investigated using a semiautomated press system, equipped with a dilatometer (see the Supporting Information, Method 1 and Figure S2).35 BTO's time-dependent shrinkage information were converted into relative density values (see the Supporting Information, Method 2) to obtain the densification curve shown in Figure 1a. In the applied conditions, BTO reaches a relative density of 90% in less than an hour (3155 s) and 95% in about 3 h (11465 s) after starting the thermal cycle (Figure 1b). The log-log plot of the strain  $(\varepsilon)$  as a function of time (t) is shown in Figure 2b. The slope of  $\log \varepsilon = f(\log t)$  gradually changes during the densification pertaining to different unfolding mechanisms. 10,36 In conventional sintering, the exponent term n is usually applied to determine power laws associated with densification mechanisms (from the relation  $\varepsilon = t^n$ ). At this time, such a full analytical consideration would be premature, as CSP with the molten hydroxides is based upon multiple coupled phenomena that are still under investigation. We do observe evolution of  $\varepsilon$ in the first 200 s, associated with the particle rearrangement step, without obvious influence on relative density (Figure 1a). This shows that the residual water adsorbed on hydroxides does not play a critical role in initiating the densification of BTO at the low temperatures. It is noted that most of the densification occurs between 200 and 3000 s, during the temperature increase and the melting of NaOH-KOH eutectic mixture (Figure 2b). The relative density evolves from 63.8 to 89.4%. Zhang et al.<sup>37</sup> have shown that large solid-solid stress concentrations could be obtained at small strains. Therefore, in the presence of a fluid, local chemical potentials are sufficiently high enough to enable a pressure solution mechanism. BTO nanoparticles are insoluble in a NaOH-KOH eutectic melt at atmospheric pressure.<sup>38</sup> However, at small strain, the locally high contact stresses between BTO nanoparticles on contact with a NaOH-KOH melt can lead to dissolution at BTO/ hydroxide melt interfaces. Insights into the detailed mechanism of chemical effects during cold sintering will be discussed with the application of ReaxFF molecular dynamics. In the later stages of densification, at larger strains (t > 3000 s), the driving force for pressure solution is lower and the process becomes precipitation controlled.

The X-ray diffraction (XRD) data shows a high phase-purity BTO after densification by CSP (Figure 1c). The cold sintered BTO ceramic is also translucent, as highlighted in Figure 1d. This reflects a high relative density (Figure 1a), together with an average grain size of  $76 \pm 27$  nm and nanopores (Figure 1e), which limits the light scattering. Despite the fact that solvents/fluxes are used as transient liquids in CSP, the efficiency of their elimination from the sample depends on their viscosity and ability to evaporate. In the BTO ceramic, residual hydroxides were observed by scanning electron microscopy (SEM)—energy-dispersive spectroscopy (EDS) analysis (Figure 1f). Onto the BTO surface, we can observe

residues composed of NaOH and small amounts of KOH. The microstructure of the NaOH/KOH residue let us assume an ongoing phase separation between the two compounds, given the morphology <sup>40</sup> of KOH. The observation of NaOH residues following a phase separation with KOH is consistent with previous observations.<sup>8</sup> Further investigation are conducted to locate KOH residues. The bright-field transmission electron microscopy (TEM) shows an image in (Figure 2a) that confirms high densification and grain structures with equilibrated achieved by CSP. No secondary phase is observable at this magnification. Figure 2c displays a HAADF-STEM micrograph focusing on a triple junction, whereas the bottom grain has been tilted to its  $\langle 001 \rangle$  zone axis. The corresponding scanning transmission electron microscopy-energy-dispersive spectroscopy (STEM-EDS) mapping is shown in Figure 2d with Ti and K elements highlighted. There is an obvious nanoscale K segregation and incorporation into the perovskite grain boundary regions and triple points in Figure 2b. Comparing Figure 2c and Figure 2d, one can note in the EDS data that the K segregation area overlaps with 3-4 atomic layers of BTO unit cells at the bottom grain as viewed here. It indicates that the formation of the grain boundary during cold sintering is accompanied by the incorporation of K-ions into the A-site of the perovskite lattice, with little evidence of the corresponding Na ions being incorporated into these regions. In summary, these observations indicate both high densities, with some preferential incorporation of K<sup>+</sup> ions into the lattice near the grain boundaries and at triple points.

Analysis of the NaOH-KOH Melting Process and Dissolution of BTO by ReaxFF Molecular Dynamics. Motivated by the complexities in the above experimental findings, we focused on atomistic level investigation of the BTO interfaces in the presence of NaOH and KOH melts. The interfaces were modeled using ReaxFF molecular dynamics (MD) simulations.<sup>41</sup> The ReaxFF has the capability of simulating elevated temperatures and pressures, which are the conditions used in CSP, and was also successfully applied to model CSP surface reaction kinetics at the metal oxide interfaces.<sup>42,43</sup> The ReaxFF force field used in this work was adapted by combining two previously developed force fields for BTO and KOH-NaOH<sup>44</sup> (see the Supporting Information, Method 4, and Figure S3).

BTO, a multi component oxide material with perovskite structure, has two possible terminations at the (001) surface, namely,  ${\rm TiO_2}$  and BaO. Both terminations have different surface potentials due to different metal and oxygen concentrations on the surface. The structure of  ${\rm TiO_2}$  terminated surface is relatively more open as both  ${\rm Ti^{4+}}$  and  ${\rm Ba^{2+}}$  ions are visible, whereas  ${\rm Ba^{2+}}$  ions are the only visible ones for BaO-terminated surfaces (see Figure S3). In this study, both surface terminations were modeled separately in addition to a mixed surface termination that included rough surfaces with a steep curvature to simulate the overall interfacial interactions of NaOH and KOH. Unless specifically mentioned, all findings of our study correspond to both surface terminations.

ReaxFF simulations demonstrate that, as soon as the temperature is increased, the molten hydroxides either create small ionic clusters and polynuclear complexes through olation (nNaOH  $\rightarrow$  Na $_n$ (OH) $_n$ , mKOH  $\rightarrow$  K $_m$ (OH) $_m$ , nNaOH + mKOH  $\rightarrow$  Na $_n$ K $_m$ (OH) $_{n+m}$ ) and oxolation (Na $_n$ (OH) $_n$   $\rightarrow$  Na $_n$ O $_{n-1}$  + H $_2$ O) reactions or dissociation of hydroxyl ions on to the BTO surface. The clustering is observed for both

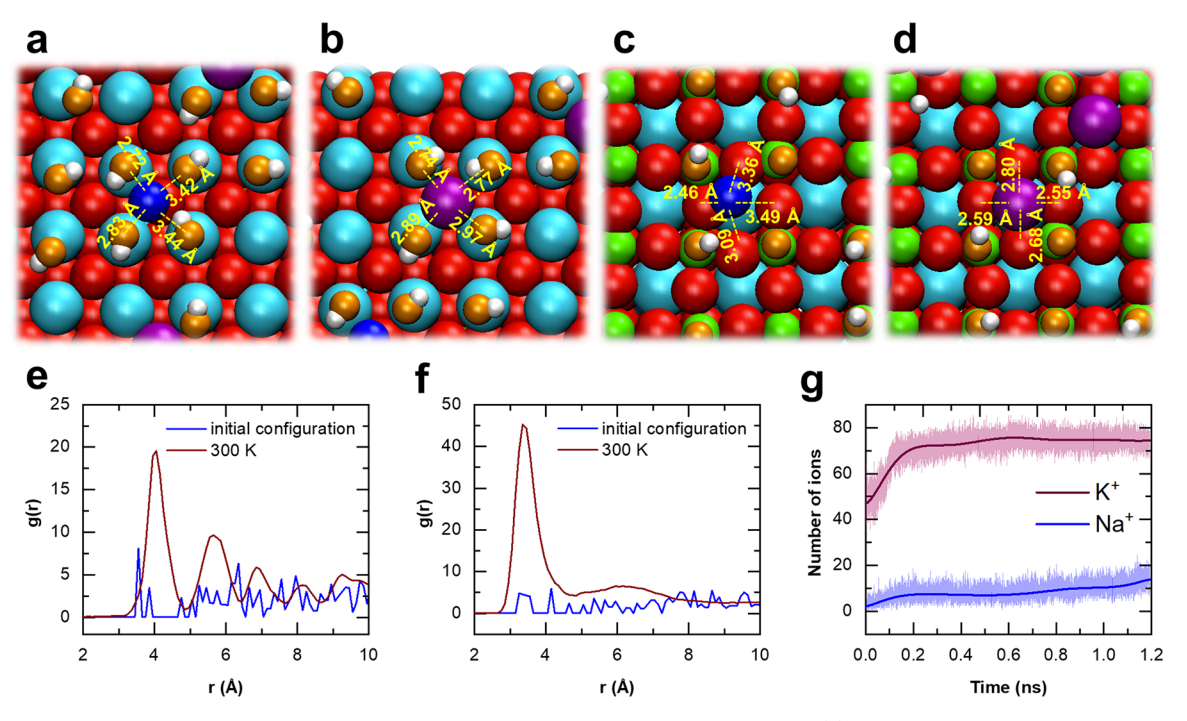


Figure 3. Representation of precipitated K<sup>+</sup> and Na<sup>+</sup> ions from molten hydroxide phase to surface. (a) Sodium adsorbed to two surface hydroxides. (b) K<sup>+</sup> bonded to four surface hydroxides. (c) Na<sup>+</sup> bonded to a surface oxygen. (d) K<sup>+</sup> bonded to four surface oxygens. Key: barium (light blue); titanium (green); potassium (purple); sodium (blue); oxygen anions on the surface (red); oxygen anions of hydroxides (orange); hydrogen atoms (white). The same colorization is used for all images. Evolution of the (e) K–K and (f) Na–Na radial distribution functions after interacted with BTO surface. The blue line represents the initial configuration, which belongs to randomly distributed ions. The red line represents the state after ions interacted with the surface at room temperature. Potassium ions adsorbed on the surface sites as can be understood from the several peeks in RDF. Sodium ions create clusters by sharing OH<sup>-</sup>. (g) Number of potassium and sodium ions within 1.5 Å from the surface during the MD simulation indicating the number of potassium ions near the surface is significantly higher than the number of sodium ions.

hydroxides. On the one hand, KOH clusters are metastable and dissociate with the increase in temperature, which may explain in part the precipitation of KOH on BTO surface. On the other hand, NaOH clusters are more stable and requires more temperature for dissociation. This can be seen in the radial distribution functions (RDFs) for both species (Figure 3e, f). Although the initial structures were prepared by randomly placing the hydroxides, the RDF of K+ show a structured distribution (Figure 3e), whereas Na<sup>+</sup> shows one peak corresponding to the clusters (Figure 3f). The clustering is also visually checked, and the simulations reveal that  $Na_n(OH)_n$  clusters changes in size with n up to 15. The clusters are formed through a series of olation and oxolation reactions as described above. The olation reactions are observed more frequently compared to oxolation reactions; however, pH may affect the frequency in experiments. As Na<sup>+</sup> and K<sup>+</sup> are both alkali metal ions, they interact with other ions mostly electrostatically, and the ionic radius of these ions determines the hydration energy due to the interactions with the dipole moment of water molecules. Because the ionic radius of Na<sup>+</sup> is smaller than K<sup>+</sup>, its charge density is higher, which strengthens the hydration energy and results in more stable clusters. The relatively more stable clustering may play a role in the formation of micrometer-size NaOH residues observed in the densified material (Figure 1f) by acting as seeds. It should be noted that because of limited simulation time scales, only reactions at a molecular level and early signs of cluster formation are accessible. However, the full extent of Na<sup>+</sup> ions crystallization up to micrometer scales remain inaccessible by ReaxFF molecular dynamics.

The precipitation behavior of alkali metal ions present in the molten flux is significantly influenced by the surface termination due to the different surface potentials. For TiO2terminated surfaces, K<sup>+</sup> ion sits on the Ba site of the lattice and is coordinated by all lattice oxygens (Figure 3d). The adsorption of Na<sup>+</sup> is much weaker than K<sup>+</sup> because Na<sup>+</sup> ions do not bind to the lattice site. However, they are strongly adsorbed to surface oxygen anions (Figure 3c) if they are not clustered. Regarding BaO-terminated surface regions, K+ ions sit on Ti sites and strongly interact with surface hydroxyl groups (Figure 3b). On the other hand, Na<sup>+</sup> ions are adsorbed to surface hydroxyls (Figure 3a) and do not sit on the Ti site. As a result, these ions are more likely to dissolve back into the solvent phase. The bond distributions of precipitated ions highlight the stronger adsorption of K<sup>+</sup> ions to surface (Figure 3d) than Na<sup>+</sup> ions (Figure 3c). Differences observed in terms of adsorption behavior explain the higher K<sup>+</sup> concentration at the interfaces experimentally confirmed by STEM-EDS (Figure 2b-d). It is also supported by the population analysis of ions adsorbed at the surface (Figure 3g) estimated from ReaxFF MD simulation outcomes (see the Supporting Information, Method 5), showing the presence of a K<sup>+</sup> ion population significantly higher than that of Na+ ions at the interface between two grains. Furthermore, the adsorption dynamics can be affected by the presence of water in the system. An additional population analysis in the presence of water molecules in the system was conducted and can be seen in the Supporting Information, Method 6 and Figure S5.

The preferential adsorption trends, as also observed experimentally, may significantly affect the dissolution dynamics. For example, as discussed above, the adsorbed

 $\mathrm{Na}^+$  ions do not complete the undercoordinated lattice structure of the surface but instead weaken the surface oxygen bonds by binding to them. On the other hand, the interactions between KOH molecule and the surface lead to the dissociation of KOH into  $\mathrm{K}^+$  and  $\mathrm{OH}^-$  ions, after which the  $\mathrm{K}^+$  ion sits on the Ba site. In a system with  $\mathrm{TiO}_2$ -terminated surface asperities and 100 KOH and 100 NaOH molecules (Figure 4a), it was observed that as a result of this preferential

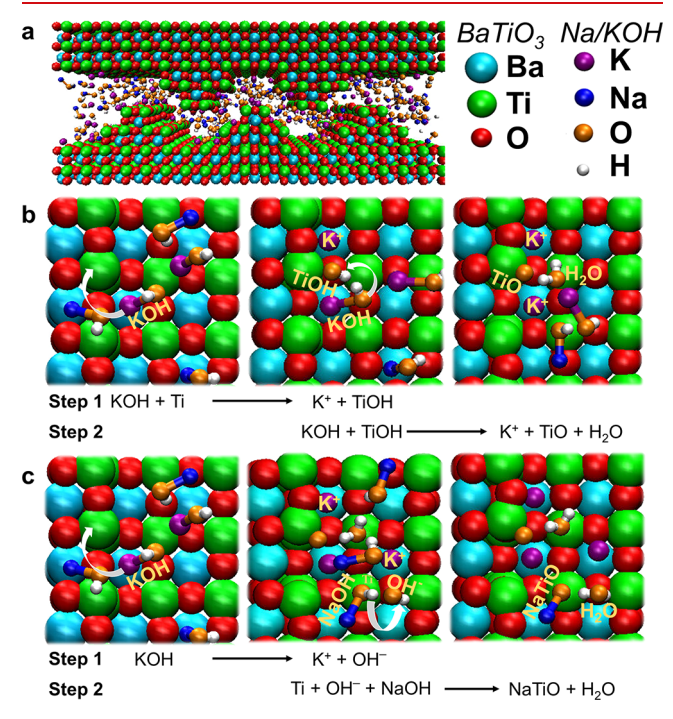


Figure 4. Representation of the major chemical reactions observed at the interface in ReaxFF MD simulations. (a) The BTO structure with asperities on the  ${\rm TiO_2}$  terminated surfaces and 100 KOH and 100 NaOH molecules at the beginning of the MD simulation. (b) First, dissociation of KOH into K<sup>+</sup> and OH<sup>-</sup> ions. K<sup>+</sup> ion sits in Ba site and OH<sup>-</sup> ion creates a bond with the  ${\rm Ti^{4+}}$  surface ion to form TiOH. In a second step, another KOH molecule participates in an oxidative dehydrogenation of TiOH to form TiO and a H<sub>2</sub>O molecule, while K<sup>+</sup> ion sits in Ba site. (c) In a first step, KOH dissociated into K<sup>+</sup> and OH<sup>-</sup> ions, following an interaction between KOH and a  ${\rm Ti^{4+}}$  surface ion. In a second step, the Ti–OH complex interacts with a NaOH molecule to form a NaTiO intermediate compound and H<sub>2</sub>O. Key: barium (light blue); titanium (green); potassium (purple); sodium (blue); oxygen atoms in BTO (red); oxygen atoms of hydroxides (orange); hydrogen atoms (white).

adsorption, the dissociated OH<sup>-</sup> ion creates a bond with surface Ti<sup>4+</sup> ion to form TiOH complex (Figure 4b, Step 1). At the same time, the adsorbed Na<sup>+</sup> ions create a NaOH complex, which interacts with surface TiOH complex and forms NaTiO complexes (Figure 4c, Step 2), which further weakens the TiO bonds at the BTO surface. An extended visualization of the chemical reactions from side and top views was provided in Supporting Information, Method 7 and Figure S6. These interactions, not dominant but frequently observed in our simulations, may experimentally correspond to the formation of a soluble Na<sub>2</sub>TiO<sub>3</sub> previously reported by Liu et al. as an intermediate compound during the flux-assisted synthesis of BaTiO<sub>3</sub>. <sup>38</sup> In addition to preferential adsorption, the presence of molten flux in the system may energetically favor the dissolution, which is shown by comparing relative energies for

dissociation of Ti<sup>4+</sup> and Ba<sup>2+</sup> ions from the BTO lattice at the surface in the presence and absence of the molten flux. The ReaxFF analyses showed that energy required for dissociation of Ti<sup>4+</sup> and Ba<sup>2+</sup> ions from BTO surface are both reduced significantly in the presence of molten fluxes (Supporting Information, Method 8 and Figure S7a-c).

#### CONCLUSION

In summary, an atomistic level description of chemical reactions at the BTO/NaOH-KOH interface was unveiled using ReaxFF molecular dynamics, and several experimentally observed phenomena were explained. Analyses revealed that very complex dynamics occur between Na+ and K+ ions and the BTO surface, subsequently enabling densification by pressure solution creep at a broader scale. During the densification, interfacial interactions lead to an incorporation of K<sup>+</sup> ions at grain boundaries, up to 3-4 atomic layers of BTO unit cells. We highlighted the dynamics of the clustering of NaOH during NaOH-KOH phase separation occurring at the precipitation stage, also observed experimentally. The phase separation was mainly due to a stability difference between Na<sup>+</sup>- and K<sup>+</sup>-clustered ions, which can be assumed to be a result of the hydration energy differences. It was also shown that there is a formation of transient complexes that enable the dissolution of both Ba and Ti from the solid during the cold sintering of BTO in molten NaOH-KOH. Therefore, using other types of molten salts, for example, alkali or alkaline earth metals with small radii (i.e., lithium, magnesium, barium, strontium), may also produce desired results. Indeed, the chemistry at the interface that enables CSP is strictly related to the interactions between the materials of interest and the molten salt ions. The nature of the molten salt to select for a given material requires a thorough understanding of these interactions and the resulting intermediate complexes.

## ASSOCIATED CONTENT

#### Supporting Information

The Supporting Information is available free of charge at https://pubs.acs.org/doi/10.1021/acs.nanolett.1c00069.

Pressure solution creep mechanism; Methods: (1) powder preparation and sintering, (2) density measurements, (3) material characterization techniques, (4) ReaxFF reactive force field method, (5) population analysis of the molten hydroxides near surface, (6) analysis of water effects on the molten hydroxide mediated CSP by ReaxFF molecular dynamics simulations, (7) visualization of the major chemical reactions at the BTO/NaOH-KOH interface in ReaxFF MD simulations, (8) analysis of effects of molten flux on dissolution of Ti<sup>4+</sup> and Ba<sup>2+</sup> ions during cold sintering (PDF)

# **■** AUTHOR INFORMATION

# **Corresponding Author**

Arnaud Ndayishimiye — Materials Research Institute, The Pennsylvania State University, University Park, Pennsylvania 16802, United States; Department of Materials Science and Engineering, The Pennsylvania State University, University Park, Pennsylvania 16802, United States; ocid.org/0000-0003-3853-8239; Phone: (814) 441-7104; Email: axn536@psu.edu

#### **Authors**

- Mert Y. Sengul Materials Research Institute, The Pennsylvania State University, University Park, Pennsylvania 16802, United States; Department of Materials Science and Engineering, The Pennsylvania State University, University Park, Pennsylvania 16802, United States; orcid.org/0000-0002-5309-0316
- Dooman Akbarian Department of Mechanical Engineering, The Pennsylvania State University, University Park, Pennsylvania 16802, United States
- Zhongming Fan Materials Research Institute, The Pennsylvania State University, University Park, Pennsylvania 16802, United States; Department of Materials Science and Engineering, The Pennsylvania State University, University Park, Pennsylvania 16802, United States
- Kosuke Tsuji Materials Research Institute, The Pennsylvania State University, University Park, Pennsylvania 16802, United States; Department of Materials Science and Engineering, The Pennsylvania State University, University Park, Pennsylvania 16802, United States
- Sun Hwi Bang Materials Research Institute, The Pennsylvania State University, University Park, Pennsylvania 16802, United States; Department of Materials Science and Engineering, The Pennsylvania State University, University Park, Pennsylvania 16802, United States
- Adri C. T. van Duin Materials Research Institute, The Pennsylvania State University, University Park, Pennsylvania 16802, United States; Department of Materials Science and Engineering and Department of Mechanical Engineering, The Pennsylvania State University, University Park, Pennsylvania 16802, United States; orcid.org/0000-0002-3478-4945
- Clive A. Randall Materials Research Institute, The Pennsylvania State University, University Park, Pennsylvania 16802, United States; Department of Materials Science and Engineering, The Pennsylvania State University, University Park, Pennsylvania 16802, United States

Complete contact information is available at: https://pubs.acs.org/10.1021/acs.nanolett.1c00069

## **Author Contributions**

<sup>†</sup>A.N. and M.Y.S. contributed equally. The manuscript was written through contributions of all authors. All authors have given approval to the final version of the manuscript.

#### **Funding**

This work was funded by the Air Force Office of Scientific Research (AFOSR), the Air Force Research Laboratory (AFRL), and the U.S. National Science Foundation (NSF).

#### **Notes**

The authors declare no competing financial interest.

## ACKNOWLEDGMENTS

This work was supported by the AFOSR (grant FA9550-19-1-0372, A.N., Z.F., C.A.R.), the AFRL (grant FA9451-16-1-0041, A.C.T.vD, D.A.), U.S. National Science Foundation (DMR-1728634: C.A.R., S.H.B; DMR-1842922 and DMR-1842952: A.C.T.vD, M.Y.S.; IIP-1841453 and 1841466 as part of the Center for Dielectric and Piezoelectric: K.T., C.A.R.).

# ABBREVIATIONS

BTO, barium titanate BaTiO<sub>3</sub> CSP, cold sintering process ReaxFF, reactive force field

#### REFERENCES

- (1) Ashby, M. F. A. First Report on Sintering Diagrams. *Acta Metall.* **1974**, 22 (3), 275–289.
- (2) German, R. M. Fundamentals of Sintering. ASM Int. Eng. Mater. Handb. 1991, 4, 260–269.
- (3) Fagereng, Å.; Den Hartog, S. A. M. Subduction Megathrust Creep Governed by Pressure Solution and Frictional-Viscous Flow. *Nat. Geosci.* **2017**, *10* (1), 51–57.
- (4) Gratier, J.-P.; Dysthe, D. K.; Renard, F. The Role of Pressure Solution Creep in the Ductility of the Earth's Upper Crust. *Adv. Geophys.* **2013**, *54*, 47–179.
- (5) Urai, J. L.; Spiers, C. J.; Zwart, H. J.; Lister, G. S. Weakening of Rock Salt by Water during Long-Term Creep. *Nature* **1986**, 324, 554–557.
- (6) Guo, J.; Guo, H.; Baker, A. L.; Lanagan, M. T.; Kupp, E. R.; Messing, G. L.; Randall, C. A. Cold Sintering: A Paradigm Shift for Processing and Integration of Ceramics. *Angew. Chem., Int. Ed.* **2016**, 55 (38), 11457–11461.
- (7) Guo, J.; Floyd, R.; Lowum, S.; Maria, J.; Herisson De Beauvoir, T.; Seo, J.-H.; Randall, C. A. Cold Sintering: Progress, Challenges, and Future Opportunities. *Annu. Rev. Mater. Res.* **2019**, 49, 275–295.
- (8) Zaengle, T. H.; Ndayishimiye, A.; Tsuji, K.; Fan, Z.; Bang, S. H.; Perini, J.; Misture, S. T.; Randall, C. A. Single-Step Densification of Nanocrystalline CeO2 by the Cold Sintering Process. *J. Am. Ceram. Soc.* **2020**, *103* (5), 2979–2985.
- (9) Ibn-Mohammed, T.; Randall, C. A.; Mustapha, K. B.; Guo, J.; Walker, J.; Berbano, S. S.; Koh, S. C. L.; Wang, D.; Sinclair, D. C.; Reaney, I. M. Decarbonising Ceramic Manufacturing: A Techno-Economic Analysis of Energy Efficient Sintering Technologies in the Functional Materials Sector. *J. Eur. Ceram. Soc.* **2019**, *39* (16), 5213–5235.
- (10) Bouville, F.; Studart, A. R. Geologically-Inspired Strong Bulk Ceramics Made with Water at Room Temperature. *Nat. Commun.* **2017**, *8*, 14655.
- (11) Hérisson de Beauvoir, T.; Sangregorio, A.; Cornu, I.; Elissalde, C.; Josse, M. Cool-SPS: An Opportunity for Low Temperature Sintering of Thermodynamically Fragile Materials. *J. Mater. Chem. C* **2018**, *6*, 2229–2233.
- (12) Herisson de Beauvoir, T.; Sangregorio, A.; Bertrand, A.; Payen, C.; Michau, D.; Chung, U.-C.; Josse, M. Cool-SPS Stabilization and Sintering of Thermally Fragile, Potentially Magnetoelectric, NH4Fe-P2O7. *Ceram. Int.* **2019**, *45*, 9674–9678.
- (13) Elissalde, C.; Chung, U.-C.; Josse, M.; Goglio, G.; Suchomel, M. R.; Majimel, J.; Weibel, A.; Soubie, F.; Flaureau, A.; Fregeac, A.; Estournès, C. Single-Step Sintering of Zirconia Ceramics Using Hydroxide Precursors and Spark Plasma Sintering below 400° C. Scr. Mater. 2019, 168, 134–138.
- (14) Goglio, G.; Ndayishimiye, A.; Largeteau, A.; Elissalde, C. View Point on Hydrothermal Sintering: Main Features, Today's Recent Advances and Tomorrow's Promises. *Scr. Mater.* **2019**, *158*, 146–152.
- (15) Yamasaki, N.; Yanagisawa, K.; Nishioka, M.; Kanahara, S. A Hydrothermal Hot-Pressing Method: Apparatus and Application. *J. Mater. Sci. Lett.* **1986**, *5*, 355–356.
- (16) Yanagisawa, K.; Nishioka, M.; Ioku, K.; Yamasaki, N. Densification of Silica Gels by Hydrothermal Hot-Pressing. *J. Mater. Sci. Lett.* **1993**, *12* (14), 1073–1075.
- (17) Onoki, T.; Hosoi, K.; Hashida, T. New Technique for Bonding Hydroxyapatite Ceramics and Titanium by Hydrothermal Hot-Pressing Method. *Scr. Mater.* **2005**, *52*, 767–770.
- (18) Kähäri, H.; Teirikangas, M.; Juuti, J.; Jantunen, H. Dielectric Properties of Lithium Molybdate Ceramic Fabricated at Room Temperature. *J. Am. Ceram. Soc.* **2014**, *97* (11), 3378–3379.
- (19) Väätäjä, M.; Kähäri, H.; Juuti, J.; Jantunen, H. Li2MoO4 -Based Composite Ceramics Fabricated from Temperature- and Atmosphere-Sensitive MnZn Ferrite at Room Temperature a. *J. Am. Ceram. Soc.* **2017**, *100*, 3626–3635.
- (20) Ndayishimiye, A.; Sengul, M. Y.; Sada, T.; Dursun, S.; Bang, S. H.; Grady, Z. A.; Tsuji, K.; Funahashi, S.; van Duin, A. C.T.; Randall,

- C. A. Roadmap for Densification in Cold Sintering: Chemical Pathways. *Open Ceram* **2020**, *2*, 100019.
- (21) Liu, X.; Fechler, N.; Antonietti, M. Salt Melt Synthesis of Ceramics, Semiconductors and Carbon Nanostructures. *Chem. Soc. Rev.* 2013, 42, 8237–8265.
- (22) Bugaris, D. E.; zur Loye, H.-C. Materials Discovery by Flux Crystal Growth: Quaternary and Higher Order Oxides Angewandte. *Angew. Chem., Int. Ed.* **2012**, *51*, 3780–3811.
- (23) Stitzer, K. E.; Smith, M. D.; zur Loye, H.-C. Crystal Growth of Ba2MOsO6 (M = Li, Na) from Reactive Hydroxide Fluxes. *Solid State Sci.* **2002**, *4*, 311–316.
- (24) Tsuji, K.; Ndayishimiye, A.; Lowum, S.; Floyd, R.; Wang, K.; Wetherington, M.; Maria, J.; Randall, C. A. Single Step Densification of High Permittivity BaTiO3 Ceramics at 300 °C. *J. Eur. Ceram. Soc.* **2020**, *40*, 1280–1284.
- (25) Lowum, S.; Floyd, R.; Maria, J. P. Hydroflux-Assisted Densification: Applying Flux Crystal Growth Techniques to Cold Sintering. J. Mater. Sci. 2020, 55, 12747–12760.
- (26) Grady, Z. M.; Tsuji, K.; Ndayishimiye, A.; Hwan-Seo, J.; Randall, C. A. Densification of a Solid-State NASICON Sodium-Ion Electrolyte below 400°C by Cold Sintering with a Fused Hydroxide Solvent. ACS Appl. Energy Mater. 2020, 3 (5), 4356–4366.
- (27) Wang, D.; Chen, J.; Wang, G.; Lu, Z.; Sun, S.; Li, J.; Jiang, J.; Zhou, D.; Song, K.; Reaney, I. M. Cold Sintered LiMgPO4 Based Composites for Low Temperature Co-Fired Ceramic (LTCC) Applications. J. Am. Ceram. Soc. 2020, 103 (11), 6237–6244.
- (28) Guo, N.; Shen, H.-Z.; Jin, Q.; Shen, P. Hydrated Precursor-Assisted Densification of Hydroxyapatite and Its Composites by Cold Sintering. *Ceram. Int.* **2021**, *47*, 14348.
- (29) Wang, D.; Li, L.; Jiang, J.; Lu, Z.; Wang, G.; Song, K.; Zhou, D.; Reaney, I. M. Cold Sintering of Microwave Dielectric Ceramics and Devices. J. Mater. Res. 2021, 36 (2), 333–349.
- (30) Dursun, S.; Tsuji, K.; Bang, S. H.; Ndayishimiye, A.; Randall, C. A. A Route towards Fabrication of Functional Ceramic/Polymer Nanocomposite Devices Using the Cold Sintering Process. *ACS Appl. Electron. Mater.* **2020**, *2* (7), 1917–1924.
- (31) Wang, D.; Siame, B.; Zhang, S.; Wang, G.; Ju, X.; Li, J.; Lu, Z.; Vardaxoglou, Y.; Whittow, W.; Cadman, D.; Sun, S.; Zhou, D.; Song, K.; Reaney, I. M. Direct Integration of Cold Sintered, Temperature-Stable Bi2Mo2O9-K2MoO4 Ceramics on Printed Circuit Boards for Satellite Navigation Antennas. *J. Eur. Ceram. Soc.* **2020**, *40* (12), 4029–4034.
- (32) Voisin, T.; Erriguible, A.; Aymonier, C. A New Solvent System: Hydrothermal Molten Salt. *Sci. Adv.* **2020**, *6*, No. eaaz7770.
- (33) Chance, W. M.; Bugaris, D. E.; Sefat, A. S.; zur Loye, H.-C. Crystal Growth of New Hexahydroxometallates Using a Hydro Fl Ux. *Inorg. Chem.* **2013**, *52*, 11723–11733.
- (34) Kishi, H.; Mizuno, Y.; Chazono, H. Base-Metal Electrode-Multilayer Ceramic Capacitors: Past, Present and Future Perspectives. *Jpn. J. Appl. Phys.* **2003**, 42 (Part 1, No. 1), 1–15.
- (35) Floyd, R.; Lowum, S.; Maria, J.-P. Instrumentation for Automated and Quantitative Low Temperature Compaction and Sintering. *Rev. Sci. Instrum.* **2019**, *90* (1–8), 055104.
- (36) Kingery, W. D. Densification during Sintering in the Presence of a Liquid Phase. I. Theory. *J. Appl. Phys.* **1959**, *30* (1959), 301–306.
- (37) Zhang, X.; Spiers, C. J.; Peach, C. J. Compaction Creep of Wet Granular Calcite by Pressure Solution at 28°C to 150°C. *J. Geophys. Res.* **2010**, *115* (1–18), B09217.
- (38) Liu, H.; Hu, C.; Wang, Z. L. Composite-Hydroxide-Mediated Approach for the Synthesis of Nanostructures of Complex Functional-Oxides. *Nano Lett.* **2006**, *6* (7), 1535–1540.
- (39) Shimooka, H.; Kohiki, S.; Kobayashi, T.; Kuwabara, M. Preparation of Translucent Barium Titanate Ceramics from Sol-Gel-Derived Transparent Monolithic Gels. *J. Mater. Chem.* **2000**, *10*, 1511–1512.
- (40) Jamie, E. A. G.; Dullens, R. P. A.; Aarts, D. G. A. L. Spinodal Decomposition of a Confined Colloid-Polymer System. *J. Chem. Phys.* **2012**, *137*, 204902.

- (41) Van Duin, A. C. T.; Dasgupta, S.; Lorant, F.; Goddard, W. A., III ReaxFF: A Reactive Force Field for Hydrocarbons. *J. Phys. Chem. A* **2001**, *105* (41), 9396–9409.
- (42) Sengul, M. Y.; Randall, C. A.; van Duin, A. C. T. ReaxFF Molecular Dynamics Study on the Influence of Temperature on Adsorption, Desorption, and Decomposition at the Acetic Acid/Water/ZnO (101 0) Interface Enabling Cold Sintering. ACS Appl. Mater. Interfaces 2018, 10, 37717–37724.
- (43) Sengul, M. Y.; Guo, J.; Randall, C. A.; Van Duin, A. C. T. Water-Mediated Surface Diffusion Mechanism Enabling the Cold Sintering Process: A Combined Computational and Experimental Study. *Angew. Chem., Int. Ed.* **2019**, 58 (36), 12420–12424.
- (44) Akbarian, D.; Yilmaz, D. E.; Cao, Y.; Ganesh, P.; Dabo, I.; Munro, J.; Van Ginhoven, R.; Van Duin, A. C. T. Understanding the Influence of Defects and Surface Chemistry on Ferroelectric Switching: A ReaxFF Investigation of BaTiO3. *Phys. Chem. Chem. Phys.* **2019**, *21* (33), 18240–18249.